Article

Synthesis of goldene comprising single-atom layer gold

Check for updates

Shun Kashiwaya [1] ✉, **Yuchen Shi** [1], **Jun Lu** [2], **Davide G. Sangiovanni** [3], **Grzegorz Greczynski** [2], **Martin Magnuson** [2], **Mike Andersson**[4], **Johanna Rosen**[1] **& Lars Hultman** [2] ✉

The synthesis of monolayer gold has so far been limited to free-standing several-atoms-thick layers, or monolayers confined on or inside templates. Here we report the exfoliation of single-atom-thick gold achieved through wet-chemically etching away Ti_3C_2 from nanolaminated Ti_3AuC_2, initially formed by substituting Si in Ti_3SiC_2 with Au. Ti_3SiC_2 is a renown MAX phase, where M is a transition metal, A is a group A element, and X is C or N. Our developed synthetic route is by a facile, scalable and hydrofluoric acid-free method. The two-dimensional layers are termed goldene. Goldene layers with roughly 9% lattice contraction compared to bulk gold are observed by electron microscopy. While ab initio molecular dynamics simulations show that two-dimensional goldene is inherently stable, experiments show some curling and agglomeration, which can be mitigated by surfactants. X-ray photoelectron spectroscopy reveals an Au $4f$ binding energy increase of 0.88 eV. Prospects for preparing goldene from other non-van der Waals Au-intercalated phases, including developing etching schemes, are presented.

The discovery of graphene created great interest in two-dimensional (2D) materials[1], but it is tricky to synthesize 2D materials comprised solely of metals. Gold nanoparticles are of interest due to their application in electronics, catalysis, photonics, sensing and biomedicine[2]. Recent advances have demonstrated that gold nanoparticle catalysts can turn plastic waste and biomass into value-added chemicals[3], and photocatalytically drive overall water splitting and hydrogen peroxide production[4]. Anisotropic gold structures are a growing area of research with various low-symmetry allotrope structures that show unique properties compared to their bulk counterparts[5]. Plasmonic properties of gold nanoparticles vary depending on geometrical properties. Cluster Au_{5-13}^- anions[6] form planar molecules due to strong relativistic effects[7] that stabilize the outer $6s$ shell and destabilize the $5d$ shell. The planarity is attributed to the unique hybridization of the half-filled $6s$ orbital with the fully occupied $5d_{z^2}$ orbital[8,9]. Atomically thin 2D Au sheets are therefore expected to offer unusual plasmonic and electronic

properties and to be potentially beneficial to photonic and medical applications such as solar energy harvesting and plasmonic photo-thermal therapies for cancer treatment[10,11]. Furthermore, the high surface-area-to-volume ratio and abundance of unsaturated atoms exposed on the surface, originating from its atomically thin 2D nature, would also contribute to enhanced catalytic properties and enrich design variation for various applications[12]. Additionally, the overall use of Au resources would be minimized due to the increase in surface-area-to-volume ratio for atomic sheets.

Inspired by the experimental realization of free-standing mono-layer iron suspended in graphene pores, theoretical studies based on density-functional theory (DFT) and ab initio molecular dynamics (AIMD) predicted stable 2D Au membranes with or without confine-ment by graphene pores[13–17], specifically, stable Au membranes sus-pended in graphene pores with diameters up to 20 nm. Notably, the DFT structural optimization indicated that the favoured 2D crystal

[1]Materials Design Division, Department of Physics, Chemistry and Biology (IFM), Linköping University, Linköping, Sweden. [2]Thin Film Physics Division, Department of Physics, Chemistry and Biology (IFM), Linköping University, Linköping, Sweden. [3]Theoretical Physics Division, Department of Physics, Chemistry and Biology (IFM), Linköping University, Linköping, Sweden. [4]Division of Sensor and Actuator Systems, Department of Physics, Chemistry and Biology (IFM), Linköping University, Linköping, Sweden. ✉e-mail: shun.kashiwaya@liu.se; lars.hultman@liu.se
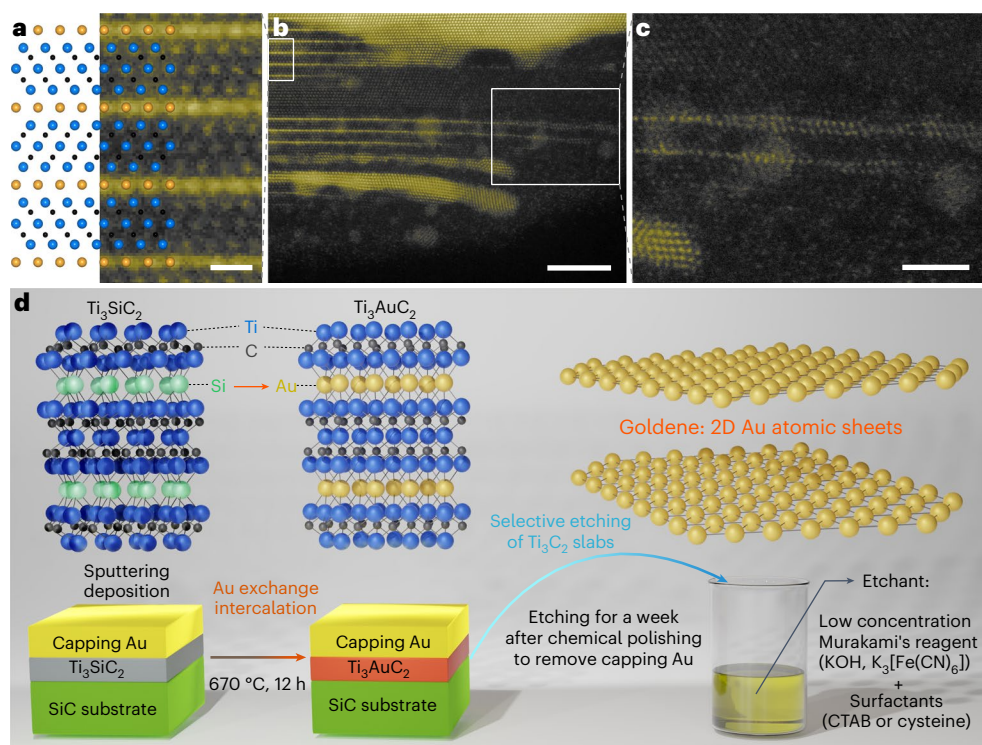
Fig. 1 | Preparation of single-atom-thick gold: goldene. a, Schematic atomic positions corresponding to a square in **b**, and HR-STEM image of Ti₃AuC₂ along with [11$\bar{2}$0] orientation marked in **b**. Yellow, blue and black balls represent Au, Ti and C atoms, respectively. Scale bar, 5 Å. **b**, Cross-sectional HR-STEM image of Ti₃AuC₂, after etching by Murakami's reagent with CTAB, where the original Ti₃AuC₂ structure remains at the left side and goldene appears at the right side of the etching frontline. Scale bar, 5 nm. **c**, Zoomed-in partly twisted goldene after etching away Ti₃C₂ slabs marked in **b**. Scale bar, 2 nm. **d**, Schematic illustration of the preparation of goldene.

would be of densely packed hexagonal structure that corresponds to the bulk monolayer of Au(111) face-centred cubic (fcc) lattice.

Epitaxial growth of single-crystal metal films has been demonstrated by numerous types of vapour deposition on lattice-matched substrates[18]. However, during deposition gold forms islands due to a strong thermodynamic tendency for coalescence. At best, this results in nanometre-thick continuous Au layers[19]. Unique synthetic routes of atomically thin gold sheets have been developed. For example, Wang et al. reported the synthesis of (001)-oriented gold nanosheets with a thickness of 0.2–0.4 nm, corresponding to 1–2-atom-thick layers diffused into a layered double-hydroxide template[20]. An attempt was made to isolate the gold sheets, but removal of the hydroxide matrix transformed the 2D Au structures into nanoparticles. Wang et al. fabricated single-atom-thick Au framed in bulk Au–Ag alloy by electron beam irradiation[21]. Similarly, Zhao et al. observed single-atom-thick Au nanoribbons suspended in graphene[22]. Bhandari et al. prepared single-atom-thick gold quantum dots stabilized on hexagonal boron nitride surfaces[23] that showed tuneable bandgaps, from 2.8 to 0.95 eV, depending on their size and shape, consistent with the DFT prediction. Forti et al. synthesized single-atom-thick Au layers, stabilized between SiC(0001) and a buffer zero-layer graphene via intercalation at elevated temperature[24]. Although both the large 2D and 3D clusters are expected to show more metallic properties as their size increases[25] and infinite free-standing Au is predicted to be metallic[15], the intercalated Au monolayer showed semiconducting properties with the valence band maximum 50 meV below the Fermi level. Recently, Sharma et al. claimed to have realized goldene by thermal dewetting of thin Au films on sapphire substrates, albeit with likely multilayers from the appearance of high-resolution scanning transmission electron microscopy (HR-STEM) images and signatures from Au islands[26]. The state-of-the-art of the thinnest free-standing '2D' gold, without physical confinements, is two-atom-thick gold nanosheets that are fabricated

via a wet-chemical route using methyl orange, which suppresses the nanosheet thickness[12]. Yet, free-standing single-atom-thick 2D Au structures at the large scale have remained unrealized.

Here, we present a synthetic route to exfoliate goldene from Ti₃AuC₂, a nanolaminated MAX phase, where M is a transition metal, A is a group A element, and X is C or N, initially formed by substituting Si in Ti₃SiC₂ with Au (ref. 27), by wet-chemically etching away the carbide slabs using Murakami's reagent with cetrimonium bromide (CTAB) or cysteine. The developed method is facile, scalable and hydrofluoric acid-free. Goldene layers with roughly 9% lattice contraction compared to bulk gold are observed by electron microscopy. Despite an intrinsic 2D stability of goldene demonstrated by AIMD simulations, experiments show some curling and agglomeration, which can be mitigated by surfactants to stabilize goldene exfoliated from Au-intercalated MAX phases. X-ray photoelectron spectroscopy (XPS) reveals Au 4f peak shifts to higher binding energy (E_b) by 0.88 eV.

Results and discussion

Preparation of goldene

Figure 1a–c shows cross-sectional HR-STEM images at 300 keV of exfoliated single-atom-thick 2D Au membranes, namely goldene, realized in this study (Supplementary Section 1). The 2D Au was achieved by etching away Ti₃C₂ slabs from nanolaminated Ti₃AuC₂ MAX-phase films by using alkaline potassium ferricyanide solution (Murakami's reagent) together with CTAB and cysteine as stabilizers (Fig. 1d). Etching without surfactants resulted in the formation of Au multilayers and clusters (Supplementary Section 2). M$_{n+1}$AX$_n$ phases (n = 1, 2, 3 or 4) are a set of intrinsically laminated ternary materials[28]. M is a transition metal, A is an element of groups 13–16 and X is carbon or nitrogen. MXene 2D ceramics are produced by etching away A layers from MAX phases, leaving M$_{n+1}$X$_n$ layers: most A elements are weakly bonded to the neighbouring M elements, while the M–X bonds are relatively strong[29,30]. Hydrofluoric
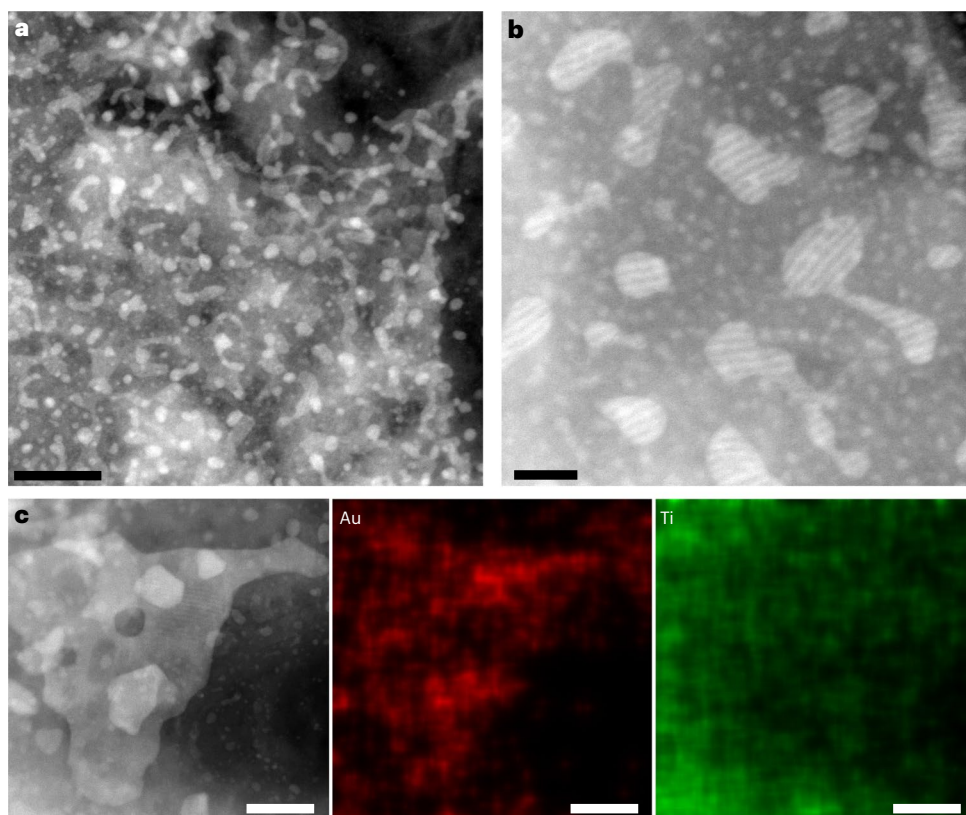
Fig. 2 | Plan-view images of goldene. a, HR-STEM image of goldene sheets that pile up on each other and get entangled. Scale bar, 30 nm. **b**, HR-STEM image of goldene sheets that subside onto the unetched residual Ti_3AuC_2, TiC seed layer below Ti_3AuC_2 or SiC substrate. Scale bar, 10 nm. **c**, HR-STEM image and energy-dispersive X-ray spectroscopy elemental mapping of goldene nanosheets. Scale bars, 30 nm.

acid is, for instance, used to selectively remove A elements from most MAX phases. Here, we invert this concept by using Murakami's reagent to etch away MX layers and leave free-standing single-atom-thick A layers. With length scale normalization from well-defined Ti_3AuC_2 lattice parameter values, we obtain Au–Au spacing of 2.62 Å in goldene (Supplementary Section 1), close to a calculated Au–Au bond length of 2.735 Å for an optimized closely packed 2D Au (Supplementary Section 3), which is roughly 9% smaller than the equilibrium interatomic distance in fcc gold (2.884 Å). Au–Au spacing values reported for subnanometre 2D Au are shorter than the typical equilibrium value found for high density and closely packed crystal structures (Supplementary Section 4) because the reduced 3D → 2D dimensionality strengthens in-plane bonding.

To elucidate the 2D morphology of goldene, we acquired plan-view HR-STEM images at 60 keV of goldene sheets obtained by etching Ti_3AuC_2 using 0.2% Murakami's reagent with CTAB for 168 h (Fig. 2). The size of the goldene sheets varies from several nanometres to 100 nm. The goldene sheets are either free-floating or stack on each other, and get entangled without causing the coalescence that would result in the formation of gold nanoparticles (Fig. 2a). This consolidates the efficacy of surfactants, which contribute to the stabilization of the goldene. Ordered patterns with 1.8–1.9 nm spans appear on goldene that subsides onto unetched residual Ti_3AuC_2 or SiC substrate (Fig. 2b,c). This is attributed to rippling of goldene, common to atomically thin materials[31] and comparable to ordered arrays of CTAB micelles on Au nanoparticles[32] in combination with rippling caused by the TEM sample preparation, as evaporating water causes the CTAB layer in between to shrink. The possibility of the 1.8–1.9 nm spacing in Fig. 2b being moiré effects between goldene sheets of different orientations or goldene on Ti_3AuC_2 or SiC could be refuted (Supplementary Section 5). Figure 2c shows STEM energy-dispersive X-ray spectroscopy mapping

of goldene sheets, demonstrating that the constituent element of the sheets is Au. Ti_3C_2 MXene and Ti oxide residuals can also be seen due to the oxidizing etchant.

Electronic properties of goldene

To gain insight into electronic properties of goldene, we performed XPS measurements on a reference sputter-etched Au foil as well as on Ti_3AuC_2 before and after etching with 0.2 and 0.5% Murakami's reagent. Goldene sheets are produced using 0.2 and 0.5% Murakami's reagent for 168 h. Figure 3 shows the corresponding Au 4f, Ti 2p and C 1s core-level XPS spectra. The Au $4f_{7/2}$ peak from the reference Au film is located at 83.96 eV, in agreement with the reference value[33]. The full-width at half-maximum (FWHM) of the Au $4f_{7/2}$ peak is 0.62 eV. The Au 4f emission for pristine Ti_3AuC_2 (before etching) shows two Au 4f doublets. The dominant doublet peaks assigned to Au atoms in the MAX phase are shifted towards a higher E_b by 0.92 eV with respect to the lower E_b pair that appears at the same E_b as the reference Au. The latter doublet is due to the partially remaining capping Au layer on the top of Ti_3AuC_2 after chemical–mechanical polishing (CMP). The E_b shift of the Au 4f peaks from Ti_3AuC_2 is attributed to the electronic charge transfer from Au to the Ti_3C_2 slabs. Such an E_b shift due to charge transfer has previously been observed between Ti, Al and C atoms in Ti_3AlC_2 and Ti_2AlC MAX phases, for which the charge redistribution was of the same extent and direction as between Ti atoms and Al atoms in TiAl alloy[34–36]. The E_b of the Au $4f_{2/7}$ XPS peaks from a Ti–Au alloy was reported to be 85 eV (ref. 35), similar to Ti_3AuC_2 in this work (Fig. 3), which further strengthens our interpretation that the high E_b doublet results from the negative charge transfer from the Au atoms to the Ti_3C_2 slabs.

A possible contribution to the observed Au 4f shift is the final state effect: the lower coordination number of Au atoms in the MAX phase than in the metallic fcc Au has a negative effect on the screening of the
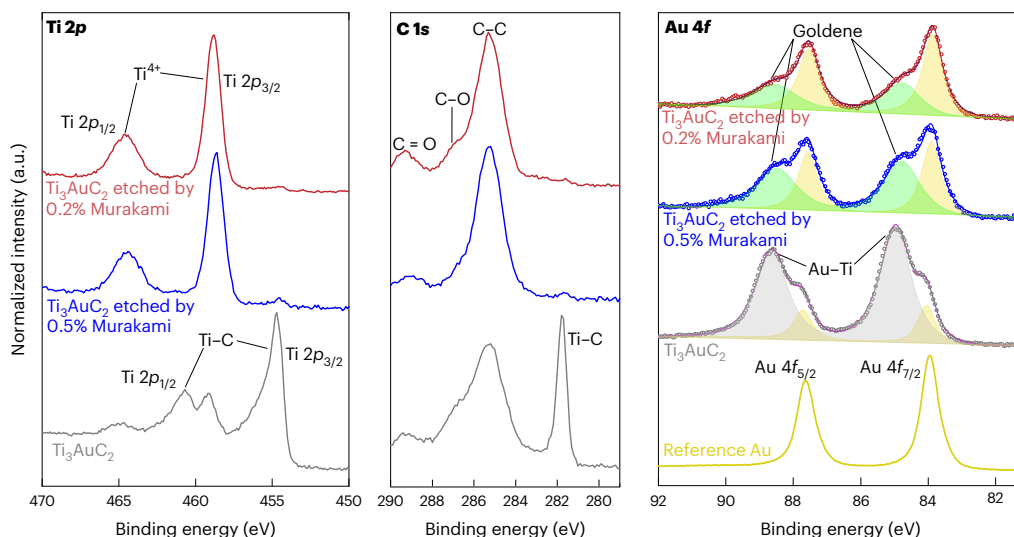
Fig. 3 | X-ray photoelectron spectra for the reference Au, Ti₃AuC₂ and goldene. Comparison of the Ti 2*p* (left), C 1*s* (middle) and Au 4*f* (right) core-level spectra of the reference sputter-cleaned Au foil as well as on Ti₃AuC₂ before and after etching by 0.2 and 0.5% Murakami's reagent with CTAB: the reference sputter-cleaned Au foil (yellow), pristine Ti₃AuC₂ (grey), goldene produced by etching Ti₃AuC₂ with 0.5% Murakami's reagent for 168 h (blue) and goldene produced by etching Ti₃AuC₂ with 0.2% Murakami's reagent for 168 h (red). For Ti₃AuC₂ before and after etching by 0.2 and 0.5% Murakami's reagent with CTAB in the Au 4*f* spectra (right), hollow dots and solid lines represent experimental data and the sum of fitted peaks: Ti–Au in Ti₃AuC₂ (grey), Au–Au in the remaining Au capping or Au particles (yellow) and Au–Au in goldene (green).

core-hole state left after the photoemission process[37,38]. Therefore, the kinetic energy of the electron escaping from the Au atoms in the MAX phase is reduced in comparison to that excited from metallic Au due to a stronger Coulomb interaction with the positively charged Au ion. The Au 4*f* peaks from Ti₃AuC₂ are also broader (FWHM = 1.10 eV versus 0.62 eV for bulk Au) due to shorter core-hole lifetimes.

The Au 4*f* spectrum from goldene produced from Ti₃AuC₂ after etching by 0.2 and 0.5% Murakami's reagent shows two doublets. The more intense pair of peaks at the lower E_b originate from residuals of the capping Au layer. The less intense doublet peaks assigned to 2D gold bonding in goldene are shifted towards a higher E_b by 0.88 eV with respect to the more intense lower E_b pair corresponding to the bulk Au. It is pertinent that the higher E_b Au 4*f* peaks originate from goldene and not from Ti₃AuC₂, as the MAX phase totally decomposes after etching. The latter is confirmed by the absence of carbidic peaks in the C 1*s* and Ti 2*p* spectra (Fig. 3). Despite the almost identical E_b position of Au 4*f* for goldene and Ti₃AuC₂, the contributions to the shift are different for goldene and Ti₃AuC₂.

Unlike the case of Ti₃AuC₂ with both the charge transfer between Au and Ti and final state effects, the shift for goldene mainly originates from the final state effects in agreement with our DFT-simulated core-level shifts (Supplementary Section 6). While the coordination number of bulk fcc Au is 12, Au in Ti₃AuC₂ forms six bonds with the surrounding Ti atoms and potentially six weaker lateral bonds with the surrounding Au atoms. Meanwhile, Au in goldene has only six or fewer lateral bonds with other Au with the shorter Au–Au distance than in the case of the bulk Au and Ti₃AuC₂. Thus, the enhanced final state effect in goldene results in the Au 4*f* shift of the same magnitude as that observed for Ti₃AuC₂. The 0.88 eV shift to higher E_b observed for goldene is smaller than shifts reported for oxidized Au species. For example, Au 4*f* shift with respect to Au⁰ ranges between 1.0 and 2.69 eV for Au¹⁻³⁺ (AuO, Au₂O and Au₂O₃); also, the shift reported for Au(OH)₃ is 2.1 eV (refs. [39–42]). Therefore, it is unlikely that the observed Au 4*f* peak shifts in the spectrum from goldene are due to Au oxidation.

AIMD for goldene
Next, we confirm the structural and dynamic stability of goldene, a monolayer of fcc Au(111), using AIMD (Supplementary Section 3).

The dynamics of 2D defect-free goldene is followed for 5 ps at 300 K. The AIMD simulations attest the dynamic stability of the stoichiometric planar motif of goldene in the hexagonal triangular structure, consistent with previous ab initio calculations and simulations (Fig. 4)[15]. However, goldene layers produced by etching show curling up and blob formation near its etched-free edges (Fig. 1 and Supplementary Section 1). Thus, we further investigated the dynamic stability of goldene considering various structures and effects of point defects: (1) infinite goldene with Au adatoms, (2) unstrained and initially strained (tension and compression) goldene nanosheets with differently oriented edges, (3) goldene nanosheets with Au vacancies and Si impurities and (4) goldene bilayers (with and without defects) with various interlayer distances (Supplementary Sections 3.2–3.6). The simulations indicate stability and planarity of goldene nanosheets cut along and ‹112› edges, for which the calculated out-of-plane vibrational amplitudes are similar to that of an infinite defect-free goldene. On the other hand, the simulations suggest that Si impurities would distort the bond network to generate ripples in the layer if located near the edges of goldene. Conversely, Au vacancies have an indirect stabilization effect by acting as trapping sites for Si impurities. Small rippling is observed in the AIMD simulations for an isolated goldene monolayer, in agreement with the experimental observation here. However, the amplitude of the ripples increases as the interlayer distance becomes smaller, which is a manifestation of mutual attraction between Au layers. Geim and collaborators recently discovered that nano-rippling is typical in graphene due to thermal fluctuations and local mechanical strain[31]. Essentially, such rippling is inherent to atomically thin free-standing 2D materials and could be beneficial to chemical reactions. Accordingly, the rippling nature of 2D Au layers observed in our STEM analysis substantiates that they are free-standing. Thus, goldene is intrinsically stable regardless of its lineaments, and the curling and blob formation observed in our experiments could be attributed to external factors related to initial Au interaction into Ti₃SiC₂ to produce Ti₃AuC₂ and subsequent etching processes, such as electron radiation damage during 300 kV STEM imaging.

Mechanistic consideration on exfoliation of goldene
We experimentally realized various forms of 2D Au layers by using different etching conditions (Supplementary Section 7). The alkaline
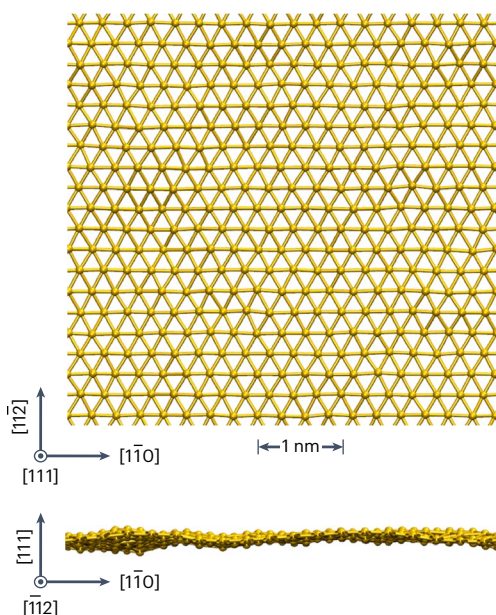
Fig. 4 | Plan and side orthographic views of a defect-free goldene monolayer. Supercell model used in AIMD simulations at 300 K. The crystallographic axes are relative to an Au(111) monolayer. The length of visible Au–Au bonds is ≤3.6 Å.

solution of potassium ferricyanide consisting of 1 g of KOH, 1 g of $K_3[Fe(CN)_6]$ and 10 ml of H_2O is conventionally called Murakami's reagent, and this concentration is referred to as 100%. Using this concentration resulted in complete decomposition of Ti_3AuC_2 into amorphous TiC and spherical Au nanoparticles; however, a 2D Au monolayer at the interface of 4H–SiC and Ti_3AuC_2 survived the aggressive etching. Besides the etchant concentration, surfactants are essential to mitigate the coalescence of goldene layers and blob formation mediated by Au adatoms or Si impurities, as predicted by the AIMD simulation (Supplementary Section 3). Combining the lower concentration of 1–3% Murakami's reagent with the usage of CTAB and cysteamine as surfactants, freestanding rippling membranes of two- and three-atom-thick 2D Au were fabricated from $Ti_3Au_nC_2$ ($n = 2$ and 3); here, blob formation at the edges of these exfoliated membranes was observed (Supplementary Section 7). The exfoliated 2D single-atom-thick Au, goldene (Fig. 1 and Supplementary Section 1), was achieved by using further lowered etchant concentrations of 0.2 and 1% Murakami's reagent together with CTAB and cysteine. CTAB is a long molecule with a length of up to 20 Å; meanwhile, the distance between Au layers within $Ti_3Au_nC_2$ is 9.28 Å. Thus, CTAB can infiltrate the Au layers exposed after etching, only in parallel to Au layers, and would block the pathway for other CTAB to enter deeper. Cysteine and cysteamine have respective lengths below 9.28 Å, smaller than CTAB, and would more easily diffuse in between Au layers, although they would eventually block the pathways. Therefore, exfoliated 2D Au first appears at edges near the etching frontline.

A mild etching is crucial for goldene derivatives from $Ti_3Au_nC_2$ compounds: the lower the concentration is, the better the yield and quality of resulting Au layers are. This trend, however, ends with concentrations of around 0.2 and 0.5% Murakami's reagent. The 0.1% concentration resulted in complete decomposition of 2D Au layers into 3D spherical nanoparticles, due to the lower concentration needing a much longer etching duration. The etchants would gradually attack the freed Au layers initially stabilized by surfactants as the radical nascent oxygen produced from the etchants eventually attacks the surfactants. Therefore, considering the balance of mildness and duration of etching, a concentration between 0.2 and 1% would be optimal for the Au layers to survive. The 0.2% Murakami's reagent with CTAB allowed exfoliated 2D Au to persist, but the blob formation at the edge of the

2D Au progresses simultaneously. Further etching would advance the blob formation at the edges, and Au atoms of the blob diffuse laterally through the layer. Therefore, we observed gold layers becoming thicker after etching for long duration (Supplementary Section 7). A previous report demonstrated the free-standing two-atom-thick Au membranes where the main structure is fcc, but hexagonal close-packed reconstruction was observed at the edges[12]. This non-fcc feature has been found to stabilize planar Au structures[43]. Appropriate selection of etchant concentrations and smaller, more suitable surfactants would trigger such reconstruction of the exfoliated 2D Au edges and enable a higher yield of goldene.

Besides etchant concentrations and surfactants, a decisive factor for preparing goldene from a series of non-van der Waals Au-intercalated MAX phases is the interlayer distance between Au layers within the MAX lattice. Our AIMD simulations demonstrate that free-standing 2D Au layers coalesce in the presence of Si impurities or if brought to within 7 Å distance of each other. However, if the separation distance increases to 10, 12 and 14 Å, the goldene–goldene interlayer interaction decreases notably (Supplementary Section 3.1). The distance between Au layers within Ti_3AuC_2 is 9.28 Å. Thus, instant interlayer interaction is expected without surfactants as soon as goldene layers are isolated from Ti_3AuC_2 during etching. Here, we produced the Au-intercalated 413 MAX phases of Ti_4AuC_3 from Ti_4SiC_3 (Supplementary Section 8). The distance between Au layers within Ti_4AuC_3 is about 12 Å. Therefore, a delay in goldene interactions after etching is expected, offering a prolonged grace period for surfactants to stabilize the goldene sheets against coalescence and thus a greater likelihood of preservation.

Conclusions
Goldene in the form of Au monolayer sheets is prepared by etching away Ti_3C_2 slabs from Ti_3AuC_2. The precise dilution of Murakami's reagent as an etchant and the appropriate use of passivating surfactants such as CTAB and cysteine are essential. Our developed processing scheme has potential for expansion of the goldene sheet area by means of etching and surfactant optimization. The template SiC(0001) wafer size that sets the area limit of growing epitaxial Ti_3SiC_2 for subsequent Au intercalation is currently 200 mm (refs. 44,45), which would give an ample allowance for practical goldene application. The produced goldene has a strongly contracted in-plane (111) lattice spacing by roughly 9% and Au 4f binding energy increase by around 0.88 eV, compared to bulk Au.

Methods
Ti_3AuC_2 films preparation
Ti_3SiC_2 films with a thickness of 60 nm were initially grown on 4H–SiC substrate via a single-step synthesis process[44]. The prepared Ti_3SiC_2 films were transferred into another deposition chamber after being etched in buffered hydrofluoric acid (NH_4F (25 g) + H_2O (50 ml) + 48% hydrofluoric acid (10 ml)) for 5 s to remove residual oxides on the surface that may hinder the next step of Au interdiffusion. The films were covered with Au to a thickness of 200 nm using magnetron sputter deposition at room temperature. The Au-covered films were transferred into a quartz tube inserted in a tube furnace for annealing at 670 °C for 12 h. The furnace was heated up at a ramping rate of 18 °C min^{-1}. To avoid oxidation of the samples, nitrogen gas was flowed through the quartz tube during annealing. At the elevated temperature, an exchange reaction of Au on top with Si within the Ti_3SiC_2 films takes place, forming Ti_3AuC_2, without destroying the original layered structure. The details of film preparation can be found elsewhere[27].
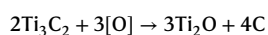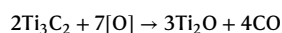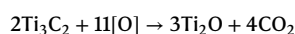
Exfoliation of goldene
Before etching off Ti_3C_2 slabs, the residual bulk Au with a thickness of up to 200 nm on the top of $Ti_3Au_nC_2$ was removed by CMP. CMP slurry was prepared by mixing fumed silica (2 g, Sigma-Aldrich), I_2 (1.2 g, Sigma-Aldrich), KI (12 g, Sigma-Aldrich), citric acid (16 g, Sigma-Aldrich)

and trisodium citrate (3.7 g, Sigma-Aldrich) in 200 ml of deionized water; here, the concentration of chemicals was optimized, substantially increased compared to the original recipe to effectively etch the thick Au reservoir[46]. The mixture was subsequently sonicated for 1 h. The CMP was performed with a polishing system, Struers Tegramin-30, while the resulting CMP slurry was dripped onto a polishing cloth (Struers MD Chem; Supplementary Section 9 shows the detailed CMP process). Goldene was produced by etching the exposed Ti_3AuC_2 films with 0.2–1.0% Murakami's reagent with surfactants of CTAB or L-cysteine for 168 h (1 week), 1 month and 2 months (Supplementary Section 10).

The etching effect produced by the Murakami's reagent originates from radical nascent oxygen [O] generated in the reaction occurring between potassium ferricyanide and alkali in close conjunction with metal carbides surface that has an attraction to oxygen[47]. When the surface is attacked by potassium ferricyanide $K_3[Fe(CN)_6]$ and KOH, the Ti_3C_2 slabs withdraw the nascent oxygen from KOH on the slab surface, and the potassium left combines with potassium ferricyanide $K_3[Fe(CN)_6]$ to form potassium ferrocyanide $K_4[Fe(CN)_6]$ (ref. [47]), according to the reaction:

$$4K_3[Fe(CN)_6] + 4KOH \rightarrow 4K_4[Fe(CN)_6] + 2H_2O + 2[O]$$
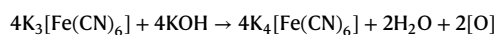
Subsequently, the Ti_3C_2 slabs are subject to the oxidative nascent oxygen as follows:

$$2Ti_3C_2 + 11[O] \rightarrow 3Ti_2O + 4CO_2$$

$$2Ti_3C_2 + 7[O] \rightarrow 3Ti_2O + 4CO$$

$$2Ti_3C_2 + 3[O] \rightarrow 3Ti_2O + 4C$$

Here, ionization tendency and susceptibility to oxidation of Ti and C are considerably higher than those of Au. Thus, Ti and C are selectively oxidized by the nascent oxygen.

Au is inert to both potassium ferricyanide and its by-product of potassium ferrocyanide under the darkness; on the other hand, the light-triggered dissolution of Au by potassium ferrocyanide was observed[48]. Even ambient light could dissolve Au in the presence of potassium ferrocyanide. Haber first reported that light irradiation could release free cyanide from potassium ferrocyanide[49] and, later, the evolution of cyanide on light exposure was also demonstrated for potassium ferricyanide[50]. The cyanide solution can dissolve gold, known as the Elsner equation, and was conventionally used in gold mining industries. In this work, preparation of the Murakami's reagent was conducted under minimum ambient light, and the etching was performed in complete darkness to avoid the evolution of cyanide that attacks Au. In summary, the susceptibility of Ti_3C_2 slabs to oxidation is greater than that of Au, which is negligible under the dark condition of the etching in this work.

To hamper the coalescence of goldene layers and stabilize them, the Murakami's reagent was mixed with various surfactants: CTAB, cysteine and cysteamine. CTAB comprises 16-carbon tails and an ammonium head group with three methyl groups and a common surfactant to tailor morphologies of Au nanoparticles. CTAB covers the Au surface as a bilayer that hinders the agglomeration of the Au nanoparticles. Cysteine and cysteamine are unique biosynthetic small molecules containing both amine and thiol functional groups. The thiols are used in a wide range of applications to stabilize and functionalize the planar gold surfaces[51]. Meanwhile, methyl and amine groups also have a strong affinity towards the Au surfaces[52].

Cysteine, of which the thiol group attaches to the Au surface, is more inert to oxidation than cysteine that is further away from the Au. This is because the oxidation of cysteine takes place preferentially by taking away the hydrogen from the thiol group to form the disulfide

cysteine. Thus, the nascent oxygen on the surface of carbides slabs would oxidize excess cysteine, which does not reach the Au surface, to form cystine. Similarly, excess cysteamine would also readily oxidize to form the disulfide cystamine by the nascent oxygen. These disulfide by-products are twice as large as cysteine and cysteamine, and there is less possibility of them diffusing in between the goldene layers during the etching of the intercalated MAX-phase host, although their affinity towards the Au surfaces would endure as the amine functional groups remain. Therefore, goldene layers were observed near the MAX edges where large surfactants can reach in between the Au layers.

Electron microscopy
Structural analysis was carried out by plan-view and cross-sectional HR-STEM with high angle annular dark field imaging using Linköping's double CS-corrected FEI Titan[3] 60–300 microscope operated at 60 and 300 keV. HR-STEM–high angle annular dark field imaging was performed using a 21.5 mrad probe convergence angle. The corresponding cross-sectional and plan-view samples were mechanically polished to a thickness of about 50 μm, followed by ion-beam milling with Ar^+ in a Gatan precision ion polishing system at 5 keV with a final polishing step at 0.8 keV of ion energy. To reduce excessive sample heating, the temperature of the sample holder was kept at about 100 K by liquid nitrogen during the ion-milling.

XPS
XPS analyses were performed in Axis Ultra DLD instrument from Kratos Analytical at a base pressure better than 1.1×10^{-9} Torr (1.5×10^{-7} Pa). Monochromatic Al Kα radiation ($hv = 1,486.6$ eV) was used with the anode power set to 150 W. All spectra were recorded at a normal emission angle. The analyser pass energy was 20 eV, which yielded a FWHM of 0.47 eV for the Ag $3d_{5/2}$ peak. The area analysed by XPS was a circle with a diameter of 100 μm. Spectrometer calibration was confirmed by measuring positions of Au $4f_{7/2}$, Ag $3d_{5/2}$ and Cu $2p_{3/2}$ peaks from sputter-etched Au, Ag and Cu samples and comparison to the recommended ISO standards for monochromatic Al Kα sources[32]. All spectra were charge-referenced to the Fermi edge.

Simulations
AIMD simulations were carried out using the VASP code implemented with the projector augmented wave method[53,54] and the generalized-gradient electronic exchange and correlation approximation[55]. An average temperature of 300 K was controlled via the Nosé–Hoover thermostat (NVT ensemble). The classical equations of motion were integrated in time steps of 1 fs. Spin-orbit coupling and relativistic effects were neglected. The van der Waals interactions were modelled using Grimme's approximation[56]. At each ionic step, the energy was calculated with accuracy of 10^{-5} eV per supercell, using a 300 eV cut-off for the planewave basis set and Γ-point sampling of the reciprocal space. Detailed information on the AIMD simulations can be found in Supplementary Section 3. Electronic structures were also calculated within the DFT framework and the projector augmented wave method. Free-standing goldene and Ti_3AuC_2 were calculated using $29 \times 29 \times 3$ k-points, while bulk Au was calculated with $29 \times 29 \times 29$ k-points sampling of the Brillouin zone using a Monkhorst–Pack scheme[57]. The energy cut-off for plane waves included in the expansion of wave functions was 400 eV. The Au $4f$ core-level shifts of free-standing goldene and Ti_3AuC_2 were calculated according to the initial state approximation[58–60] (Supplementary Section 6).

Data availability
The data supporting the findings of this work are available within the article, the corresponding Supplementary Information and the public data repository figshare: https://doi.org/10.6084/m9.figshare.24584940 (ref. [61]).

References

1. Shanmugam, V. et al. A review of the synthesis, properties, and applications of 2D materials. *Part. Part. Syst. Charact.* **39**, 2200031 (2022).

2. Li, N., Zhao, P. & Astruc, D. Anisotropic gold nanoparticles: synthesis, properties, applications, and toxicity. *Angew. Chem. Int. Ed.* **53**, 1756–1789 (2014).

3. Miura, H. et al. Diverse alkyl–silyl cross-coupling via homolysis of unactivated C (sp^3)–O bonds with the cooperation of gold nanoparticles and amphoteric zirconium oxides. *J. Am. Chem. Soc.* **145**, 4613–4625 (2023).

4. Tada, H. Overall water splitting and hydrogen peroxide synthesis by gold nanoparticle-based plasmonic photocatalysts. *Nanoscale Adv.* **1**, 4238–4245 (2019).

5. Hong, X., Tan, C., Chen, J., Xu, Z. & Zhang, H. Synthesis, properties and applications of one- and two-dimensional gold nanostructures. *Nano Res.* **8**, 40–55 (2015).

6. Goldsmith, B. R. et al. Two-to-three dimensional transition in neutral gold clusters: the crucial role of van der Waals interactions and temperature. *Phys. Rev. Mater.* **3**, 016002 (2019).

7. Pyykko, P. Relativistic effects in structural chemistry. *Chem. Rev.* **88**, 563–594 (1988).

8. Fernández, E. M., Soler, J. M., Garzón, I. L. & Balbás, L. C. Trends in the structure and bonding of noble metal clusters. *Phys. Rev. B* **70**, 165403 (2004).

9. Häkkinen, H., Moseler, M. & Landman, U. Bonding in Cu, Ag, and Au clusters: relativistic effects, trends, and surprises. *Phys. Rev. Lett.* **89**, 033401 (2002).

10. Baffou, G., Cichos, F. & Quidant, R. Applications and challenges of thermoplasmonics. *Nat. Mater.* **19**, 946–958 (2020).

11. Graziano, G. All-plasmonic water splitting. *Nat. Nanotechnol.* **16**, 1053 (2021).

12. Ye, S. et al. Sub-nanometer thick gold nanosheets as highly efficient catalysts. *Adv. Sci.* **6**, 1900911 (2019).

13. Ono, S. Dynamical stability of two-dimensional metals in the periodic table. *Phys. Rev. B* **102**, 165424 (2020).

14. Koskinen, P. & Korhonen, T. Plenty of motion at the bottom: atomically thin liquid gold membrane. *Nanoscale* **7**, 10140–10145 (2015).

15. Yang, L.-M., Dornfeld, M., Frauenheim, T. & Ganz, E. Glitter in a 2D monolayer. *Phys. Chem. Chem. Phys.* **17**, 26036–26042 (2015).

16. Yang, L.-M., Ganz, A. B., Dornfeld, M. & Ganz, E. Computational study of quasi-2D liquid state in free standing platinum, silver, gold, and copper monolayers. *Condens. Matt.* **1**, 1 (2016).

17. Nevalaita, J. & Koskinen, P. Stability limits of elemental 2D metals in graphene pores. *Nanoscale* **11**, 22019–22024 (2019).

18. Campbell, C. T. Ultrathin metal films and particles on oxide surfaces: structural, electronic and chemisorptive properties. *Surf. Sci. Rep.* **27**, 1–111 (1997).

19. Norrman, S., Andersson, T., Granqvist, C. & Hunderi, O. Optical properties of discontinuous gold films. *Phys. Rev. B* **18**, 674 (1978).

20. Wang, L. et al. Two-dimensional gold nanostructures with high activity for selective oxidation of carbon–hydrogen bonds. *Nat. Commun.* **6**, 6957 (2015).

21. Wang, X., Wang, C., Chen, C., Duan, H. & Du, K. Free-standing monatomic thick two-dimensional gold. *Nano Lett.* **19**, 4560–4566 (2019).

22. Zhao, L., Ta, H. Q., Mendes, R. G., Bachmatiuk, A. & Rummeli, M. H. In situ observations of freestanding single-atom-thick gold nanoribbons suspended in graphene. *Adv. Mater. Interfaces* **7**, 2000436 (2020).

23. Bhandari, S. et al. Two-dimensional gold quantum dots with tunable bandgaps. *ACS Nano* **13**, 4347–4353 (2019).

24. Forti, S. et al. Semiconductor to metal transition in two-dimensional gold and its van der Waals heterostack with graphene. *Nat. Commun.* **11**, 2236 (2020).

25. Natarajan, G., Mathew, A., Negishi, Y., Whetten, R. L. & Pradeep, T. A unified framework for understanding the structure and modifications of atomically precise monolayer protected gold clusters. *J. Phys. Chem. C* **119**, 27768–27785 (2015).

26. Sharma, S. K., Pasricha, R., Weston, J., Blanton, T. & Jagannathan, R. Synthesis of self-assembled single atomic layer gold crystals-goldene. *ACS Appl. Mater. Interfaces* **14**, 54992–55003 (2022).

27. Fashandi, H. et al. Synthesis of Ti_3AuC_2, $Ti_3Au_2C_2$ and Ti_3IrC_2 by noble metal substitution reaction in Ti_3SiC_2 for high-temperature-stable Ohmic contacts to SiC. *Nat. Mater.* **16**, 814–818 (2017).

28. Lei, X. & Lin, N. Structure and synthesis of MAX phase materials: a brief review. *Crit. Rev. Solid State Mater. Sci.* **47**, 736–771 (2022).

29. Lim, K. R. G. et al. Fundamentals of MXene synthesis. *Nat. Synth.* **1**, 601–614 (2022).

30. Naguib, M. et al. Two-dimensional nanocrystals produced by exfoliation of Ti_3AlC_2. *Adv. Mater.* **23**, 4248–4253 (2011).

31. Sun, P. et al. Unexpected catalytic activity of nanorippled graphene. *Proc. Natl Acad. Sci. USA* **120**, e2300481120 (2023).

32. Li, R. et al. Study on the assembly structure variation of cetyltrimethylammonium bromide on the surface of gold nanoparticles. *ACS Omega* **5**, 4943–4952 (2020).

33. International Organization for Standardization. *Surface Chemical Analysis—X-ray Photoelectron Spectrometers—Calibration of Energy Scales*. ISO 15472:2010 (ISO, 2020).

34. Näslund, L.-Å., Persson, P. O. & Rosen, J. X-ray photoelectron spectroscopy of Ti_3AlC_2, $Ti_3C_2T_z$, and TiC provides evidence for the electrostatic interaction between laminated layers in MAX-phase materials. *J. Phys. Chem. C* **124**, 27732–27742 (2020).

35. Svanidze, E. et al. An itinerant antiferromagnetic metal without magnetic constituents. *Nat. Commun.* **6**, 7701 (2015).

36. Magnuson, M. et al. Electronic structure and chemical bonding in Ti_2AlC investigated by soft x-ray emission spectroscopy. *Phys. Rev. B* **74**, 195108 (2006).

37. Wertheim, G., DiCenzo, S. & Youngquist, S. Unit charge on supported gold clusters in photoemission final state. *Phys. Rev. Lett.* **51**, 2310 (1983).

38. DiCenzo, S., Berry, S. & Hartford, E. Jr Photoelectron spectroscopy of single-size Au clusters collected on a substrate. *Phys. Rev. B* **38**, 8465 (1988).

39. de Anda Villa, M. et al. Assessing the surface oxidation state of free-standing gold nanoparticles produced by laser ablation. *Langmuir* **35**, 11859–11871 (2019).

40. Klyushin, A. Y., Rocha, T. C., Hävecker, M., Knop-Gericke, A. & Schlögl, R. A near ambient pressure XPS study of Au oxidation. *Phys. Chem. Chem. Phys.* **16**, 7881–7886 (2014).

41. Juodkazis, K., Juodkazyt, J., Jasulaitien, V., Lukinskas, A. & Šebeka, B. XPS studies on the gold oxide surface layer formation. *Electrochem. Commun.* **2**, 503–507 (2000).

42. Krozer, A. & Rodahl, M. X-ray photoemission spectroscopy study of UV/ozone oxidation of Au under ultrahigh vacuum conditions. *J. Vacuum Sci. Technol. A* **15**, 1704–1709 (1997).

43. Kondo, Y. & Takayanagi, K. Gold nanobridge stabilized by surface structure. *Phys. Rev. Lett.* **79**, 3455 (1997).

44. Fashandi, H. et al. Single-step synthesis process of Ti_3SiC_2 ohmic contacts on 4H-SiC by sputter-deposition of Ti. *Scr. Mater.* **99**, 53–56 (2015).

45. Musolino, M. et al. Paving the way toward the world's first 200mm SiC pilot line. *Mater. Sci. Semicond. Process.* **135**, 106088 (2021).

46. Miller, M. S., Ferrato, M.-A., Niec, A., Biesinger, M. C. & Carmichael, T. B. Ultrasmooth gold surfaces prepared by chemical mechanical polishing for applications in nanoscience. *Langmuir* **30**, 14171–14178 (2014).

47. Groesbeck, E. C. *Metallographic Etching Reagents. Part III. For Alloy Steels* (US Department of Commerce, Bureau of Standards, 1925).

48. Chen, W. D., Kang, S.-K., Stark, W. J., Rogers, J. A. & Grass, R. N. The light triggered dissolution of gold wires using potassium ferrocyanide solutions enables cumulative illumination sensing. *Sens. Actuat. B* **282**, 52–59 (2019).

49. Haber, F. Nachweis und Fällung der Ferroionen in der Wässerigen Lösung des Ferrocyankaliums. *Z. Elektrochem. Angew. Phys. Chem.* **11**, 846–850 (1905).

50. Yu, X., Peng, X. & Wang, G. Photo induced dissociation of ferri and ferro cyanide in hydroponic solutions. *Int. J. Environ. Sci. Technol.* **8**, 853–862 (2011).

51. Häkkinen, H. The gold–sulfur interface at the nanoscale. *Nat. Chem.* **4**, 443–455 (2012).

52. Abild-Pedersen, F. et al. Scaling properties of adsorption energies for hydrogen-containing molecules on transition-metal surfaces. *Phys. Rev. Lett.* **99**, 016105 (2007).

53. Kresse, G. & Joubert, D. From ultrasoft pseudopotentials to the projector augmented-wave method. *Phys. Rev. B* **59**, 1758–1775 (1999).

54. Kresse, G. & Furthmuller, J. Efficient iterative schemes for ab initio total-energy calculations using a plane-wave basis set. *Phys. Rev. B* **54**, 11169–11186 (1996).

55. Perdew, J. P., Burke, K. & Ernzerhof, M. Generalized gradient approximation made simple. *Phys. Rev. Lett.* **77**, 3865–3868 (1996).

56. Grimme, S. Semiempirical GGA-type density functional constructed with a long-range dispersion correction. *J. Comput. Chem.* **27**, 1787–1799 (2006).

57. Monkhorst, H. J. & Pack, J. D. Special points for Brillouin-zone integrations. *Phys. Rev. B* **13**, 5188 (1976).

58. Köhler, L. & Kresse, G. Density functional study of CO on Rh(111). *Phys. Rev. B* **70**, 165405 (2004).

59. Lizzit, S. et al. Surface core-level shifts of clean and oxygen-covered Ru (0001). *Phys. Rev. B* **63**, 205419 (2001).

60. Tal, A. A., Olovsson, W. & Abrikosov, I. A. Origin of the core-level binding energy shifts in Au nanoclusters. *Phys. Rev. B* **95**, 245402 (2017).

61. Kashiwaya, S. et al. *Goldene—exfoliated single-atom-thick sheets of gold. figshare* https://doi.org/10.6084/m9.figshare.24584940 (2024).

Acknowledgements

Author contributions

L.H. conceived and supervised the study. J.R., S.K. and L.H. designed the study. Implementation was made by S.K. (MAX-phase film growth, intercalation experiments, etching and surfactant protocols and STEM sample preparation), Y.S. (MAX-phase film growth, intercalation experiments and STEM sample preparation), M.A. (Au film growth), J.L. (STEM analysis), G.G. (XPS), M.M. (DFT-simulated XPS core-level shifts) and D.G.S. (AIMD simulations). S.K., Y.S., J.L., G.G., M.M. and D.G.S. performed the data analysis. S.K., L.H. and D.G.S. wrote the paper. All authors contributed to the final editing of the paper.

Funding

Competing interests

The authors declare no competing interests.

Additional information

Supplementary information The online version contains supplementary material available at https://doi.org/10.1038/s44160-024-00518-4.

Correspondence and requests for materials should be addressed to Shun Kashiwaya or Lars Hultman.

Peer review information *Nature Synthesis* thanks Kevin Critchley, Ivan Shtepliuk and the other, anonymous, reviewer(s) for their contribution to the peer review of this work. Primary Handling Editor: Alexandra Groves, in collaboration with the *Nature Synthesis* team.

Reprints and permissions information is available at www.nature.com/reprints.

Publisher's note Springer Nature remains neutral with regard to jurisdictional claims in published maps and institutional affiliations.